Electromagnetic Interference Caused by Parasitic Electric-line Current on a Digital Module in a Closed Cabinet

JAEYUL CHOO [ID]1, JONG-EON PARK [ID]2, HOSUNG CHOO [ID]3, AND YONG-HWA KIM [ID]4

[1]Department of Instrumentation, Control, and Electrical System, Korea Institute of Nuclear Safety, Daejeon 34142, South Korea
[2]Metamaterial Electronic Device Research Center, Hongik University, Seoul 04066, South Korea
[3]School of Electronic and Electrical Engineering, Hongik University, Seoul 04066, South Korea
[4]Department of Electronic Engineering, Myongji University, Yongin 17058, South Korea

Corresponding author: Yong-Hwa Kim (yongkim@mju.ac.kr)

ABSTRACT This paper conducts an electromagnetic analysis of the closed cabinet used for instrumentation and control in nuclear power plants for the case of a parasitic electric-line current that is undesirably generated onto an interior digital module. Based on the Helmholtz equation in conjunction with both the separation of variables and superposition principle, we employed a mode-matching method to obtain the analytic solution to an electromagnetic interference problem. Using modal coefficients from a set of simultaneous equations by enforcing boundary conditions, we computationally derive electromagnetic-field distributions in terms of various geometric parameters. The results provide us with information useful for estimating the level of influence of the undesired current source on the adjacent digital modules.

INDEX TERMS Electric-line current, electromagnetic interference, mode-matching method.

I. INTRODUCTION

Generally, a cabinet is used to install devices such as a programmable logic controller (PLC) for instrumentation and control (I&C) systems in nuclear power plants. The recent digitalization of I&C systems in nuclear power plants has enabled numerous analog-type devices to be integrated, resulting in simplification and reduction of fabrication cost. However, such digitalization of I&C systems simultaneously requires immunity to electromagnetic (EM) interference for its own functionality [1]–[8]. In particular, a cabinet-including device with digital components and modules, associated with the safety function of a nuclear power plant, should stably operate without functional deterioration against EM interference (EMI) [9]–[11].

To take precautionary measures against EMI, electromagnetic scattering analysis of an open cabinet has been performed for the event of an external electromagnetic wave with either transverse electric or magnetic mode approaching an open cabinet [4], [5], [7]. However, there have been

few attempts to investigate the effects of EMI caused by an unwanted current source on a digital module installed in a closed cabinet. Thus, we conduct a mode-matching analysis of a closed cabinet under the assumption that an unwanted electric-line current is formed onto a digital module. The resulting electric- and magnetic-field distributions corresponding to the variation in geometric parameters provide us with useful information on how much an undesired electric-line current electromagnetically affects nearby digital modules, which may result in the deterioration of the safety function of a nuclear power plant. In addition, the examined results simultaneously offer instructive insight into the chassis used to install the digital modules. We organize the rest of this paper as follows. In Section 2, we explain the mode-matching formulation. Then, we present the computed results and the conclusion of the mode-matching analysis in Sections 3 and 4, respectively.

II. MODE-MATCHING FORMULATION

Fig. 1(a) shows the I&C cabinet, including the PLC that is utilized to perform safety functions in a nuclear power plant.
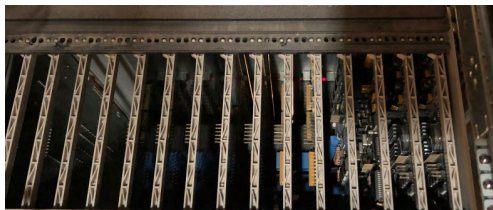
FIGURE 1. (a) Overall view of closed cabinets containing PLCs. (b) Front view of the PLC in a closed cabinet. (c) Installed configuration of digital modules comprising the PLC.

The PLC is composed of multiple digital modules made up of printed circuit boards (PCBs) and a metallic chassis for the installation of the digital modules, as shown in Fig. 1(b). In detail, the digital modules parallel to each other are inserted into the metallic chassis with a periodic separation distance, as illustrated in Fig. 1(c). Although the method to reduce EMI is properly considered in the design of the digital module, the occurrence of a parasitic current in the digital modules is inevitable, which then leads the EMI with adjacent digital modules. Even worse, the parallel digital modules can unintentionally work as an EMI generator because the parallel metallic plates (PCB grounds) guide and then excite the EM wave generated by the parasitic current source. Therefore, an EM analysis of the closed cabinet including the PLC is required to predict the effect of the EMI caused by the
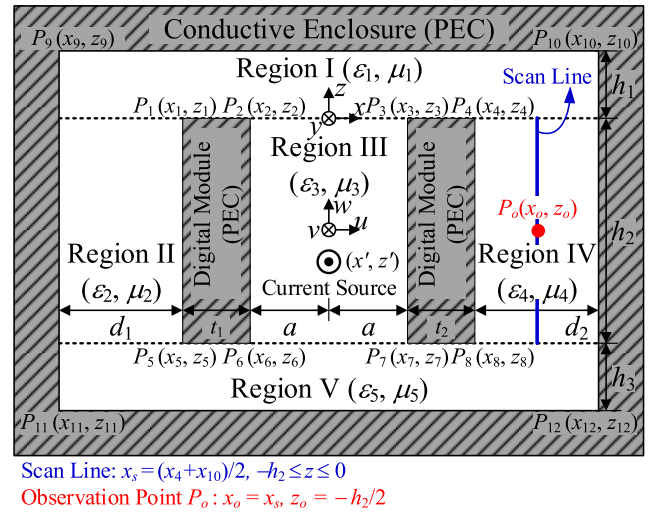

Scan Line: $x_s = (x_4 + x_{10})/2, \; -h_2 \leq z \leq 0$
Observation Point $P_o : x_o = x_s, \; z_o = -h_2/2$

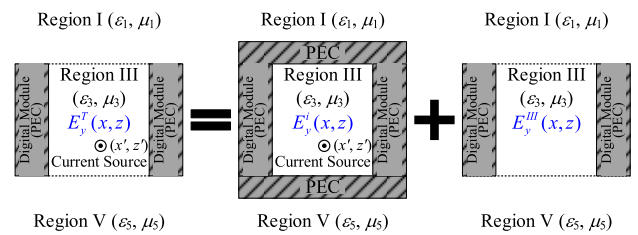**FIGURE 2.** Configuration of the closed cabinet including digital modules (top view).

FIGURE 3. Superposition principle for expression of EM field in region III.

parasitic current source. To analyze the aforementioned EM problem, we employ a mode-matching method characterized by efficient computation by fast convergence in series solutions.

First, we produce a simple model of the closed cabinet (conductive enclosure) with both installed digital modules as a rectangular cavity and thin plates made of a perfect electric conductor (PEC).

Fig. 2 shows the configuration of the closed cabinet including digital modules as a cross-section (top view) in which we assume that the closed cabinet and both digital modules are infinitely long along the *y*-axis. In Fig. 2, both digital modules are separated from each other by a distance of $2a$ and from the conducting enclosure (PEC) of the closed cabinet by distances of h_1, h_3, d_1, and d_2. To express the parasitic current source, we consider an electric-line current with strength J (A/m^2) located at $(x = x', z = z')$. To formulate scattered electric and magnetic fields, we divide the overall region in the cabinet into 5 subregions (Regions I–V), where we also set 12 points from P_1 to P_{12} as our measurement and both the permittivity (ε_n) and permeability (μ_n) in region n (n = I, II, III, IV, or V), respectively. In Fig. 2, we define a scan line ($x = x_s = (x_4 + x_{10})/2, \; -h_2 \leq z \leq 0$) and an observation point $P_o(x = x_o = x_s, z = z_o = -h_2/2)$ to quantitatively evaluate the EMI influence on an adjacent space.

We employ the superposition principle to represent the EM field in region III, as shown in Fig. 3. We separately consider

two cases, one in which an electric-line current exists in region III enclosed by PEC and one in which the current does not exist in region III, as illustrated in Fig. 3 [12]–[13]. For the existing current case, the incident electric field (E_y^i) is expressed as (1). For the other case, we can express the electric field (E_y^{III}) by the Helmholtz equation as (2). As a result, we can obtain the total electric field (E_y^T) in region III as the sum of E_y^i and E_y^{III} ($E_y^T = E_y^i + E_y^{III}$). For the electric field in other regions, we also derive expressions for the electric field in regions I, II, IV, and V based on the Helmholtz equation in conjunction with the separation of variables, as (3)–(6) [13].

$$E_y^i(x,z) = \begin{cases} \sum_{m_3=1}^{M_3} -i\omega\mu_3 J\chi_{m_3}(x',x)\nu_{m_3}(z',z), & z' < z \leq 0 \\ \sum_{m_3=1}^{M_3} -i\omega\mu_3 J\chi_{m_3}(x',x)\nu_{m_3}(z,z'), & -h_2 \leq z < z' \end{cases} \tag{1}$$

$$E_y^{III}(x,z) = i\omega \sum_{m_3=1}^{M_3} \sin\gamma_{m_3}(x-x_2) \times (A_{m_3}\sin\xi_{m_3}z + B_{m_3}\cos\xi_{m_3}z) \tag{2}$$

$$E_y^I(x,z) = i\omega \sum_{m_1=1}^{M_1} A_{m_1}\sin\gamma_{m_1}(x-x_9)\sin\xi_{m_1}(z-z_9) \tag{3}$$

$$E_y^{II}(x,z) = i\omega \sum_{m_2=1}^{M_2} \sin\gamma_{m_2}(x-x_9) \times (A_{m_2}\sin\xi_{m_2}z + B_{m_2}\cos\xi_{m_2}z) \tag{4}$$

$$E_y^{IV}(x,z) = i\omega \sum_{m_4=1}^{M_4} \sin\gamma_{m_4}(x-x_4) \times (A_{m_4}\sin\xi_{m_4}z + B_{m_4}\cos\xi_{m_4}z) \tag{5}$$

$$E_y^V(x,z) = i\omega \sum_{m_5=1}^{M_5} A_{m_5}\sin\gamma_{m_5}(x-x_9)\sin\xi_{m_5}(z-z_{11}) \tag{6}$$

where $\nu_{m_3}(\alpha,\beta) = \sin\xi_{m_3}(\alpha+h_2)\sin\xi_{m_3}\beta$, $\chi_{m_3}(\alpha,\beta) = \sin\gamma_{m_3}(\alpha+a)\sin\gamma_{m_3}(\beta+a)/(a\xi_{m_3}\sin\xi_{m_3}h_2)$, M_n represents the maximum mode number in region n (n = I, II, III, IV, or V), $\gamma_{m_1} = m_1\pi/(2a+t_1+t_2+d_1+d_2)$, $\gamma_{m_2} = m_2\pi/d_1$, $\gamma_{m_3} = m_3\pi/2a$, $\gamma_{m_4} = m_4\pi/d_2$, $\gamma_{m_5} = m_5\pi/(2a+t_1+t_2+d_1+d_2)$, and ξ_{m_n} in region n (n = I, II, III, IV, or V) is defined as $\xi_{m_n} = \sqrt{\omega^2\varepsilon_n\mu_n - \gamma_{m_n}^2}$. Note that the representation of the magnetic field (H_x) in each region can be derived using the relation of $H_x = (i/\omega\mu)\cdot(dE_y/dz)$.

Next, the unknown modal coefficients A_{m_1}, A_{m_2}, A_{m_3}, A_{m_4}, A_{m_5}, B_{m_2}, B_{m_3}, B_{m_4} in (2)–(6) can be determined by enforcing the boundary conditions on the continuities of the tangential electric and magnetic fields (E_y and H_x) at $z = 0$ and $z = -h_2$. The continuities of the tangential electric and

magnetic fields at $z = 0$ are expressed as follows,

$$E_y^I(x,z)\Big|_{z=0} = \begin{cases} E_y^{II}(x,z)\Big|_{z=0}, & x_9 < x < x_1 \\ 0, & x_1 < x < x_2 \\ E_y^i(x,z)\Big|_{z=0} + E_y^{III}(x,z)\Big|_{z=0}, & x_2 < x < x_3 \\ 0, & x_3 < x < x_4 \\ E_y^{IV}(x,z)\Big|_{z=0}, & x_4 < x < x_{10} \end{cases} \tag{7}$$

$$H_x^I(x,z)\Big|_{z=0} = H_x^{II}(x,z)\Big|_{z=0}, \quad x_9 < x < x_1 \tag{8}$$

$$H_x^I(x,z)\Big|_{z=0} = H_x^i(x,z)\Big|_{z=0} + H_x^{III}(x,z)\Big|_{z=0}, \quad x_2 < x < x_3 \tag{9}$$

$$H_x^I(x,z)\Big|_{z=0} = H_x^{IV}(x,z)\Big|_{z=0}, \quad x_4 < x < x_{10}. \tag{10}$$

The boundary conditions on the continuities of the tangential electric and magnetic fields at $z = -h_2$ are analogous to (7)–(10). The results from the enforcement of the boundary conditions constitute a set of simultaneous equations to determine the unknown modal coefficients. Note that the specific procedure to build a set of simultaneous equations from the boundary condition is similar to those of [4]–[5], [12]. The specific derivation of the boundary conditions (7) and (8) is shown in the Appendix.

III. COMPUTED RESULTS

Before obtaining the computed results regarding the EMI from the electric-line current, we first checked the convergence behavior of our series solution in each region by examining the variation in the relative error (η) corresponding to the increase in the maximum mode number [14]. The expression of the relative error at observation point P_{ob} ($x = x_{ob}$, $z = z_{ob}$) in region n is

$$\eta_n = \left| \frac{E_y^n(x_{ob},z_{ob})\Big|_{M=M_n} - E_y^n(x_{ob},z_{ob})\Big|_{M=h}}{E_y^n(x_{ob},z_{ob})\Big|_{M=M_n}} \right| \tag{11}$$

where $h = 1, 2, 3, \cdots, M_n$ for region n.

We investigated the relative errors at the observation points P_{ob} in regions I, II, and III, as shown in Fig. 4, where the observation points for regions I, II, and III are ($x_{ob} = x_1$, $z_{ob} = z_{10}/2$), ($x_{ob} = (x_1+x_9)/2$, $z_{ob} = (z_1+z_5)/2$), ($x_{ob} = (x_2+x_3)/2$, $z_{ob} = z_4/4$), respectively. The results show that the relative errors substantially decrease to less than 1% as the maximum mode number increases in each region, which validates the performed formulation and computation for this EM analysis.

We then computed the electric-field strength in a closed cabinet at 2 GHz and 4 GHz when the electric-line current
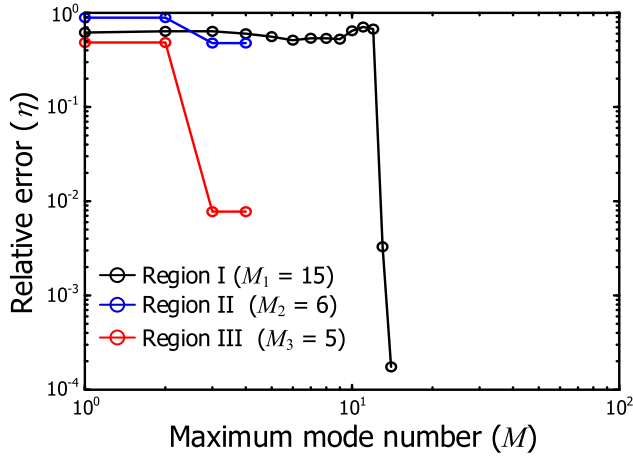
FIGURE 4. Relative errors of electric-field strength at the observation points $P_{ob}(x_{ob}, z_{ob})$ in regions I, II, and III while the maximum mode number increases, where we set geometrical parameters are $d_1 = 230$ mm, $d_2 = 170$ mm $t_1 = t_2 = 50$ mm, $a = 80$ mm, $h_1 = 250$ mm, $h_2 = 100$ mm, $h_3 = 50$ mm, $x' = 0$ mm, $z' = -50$ mm, $\varepsilon_1 = \varepsilon_2 = \varepsilon_3 = \varepsilon_4 = \varepsilon_5 = 8.854 \times 10^{-12}$ F/m, $\mu_1 = \mu_2 = \mu_3 = \mu_4 = \mu_5 = 4\pi \times 10^{-7}$ H/m, and frequency = 3 GHz.

($J = 0.001$ A/m²) is closed to the digital module in region III ($x = x' = 70$ mm, $z = z' = -100$ mm), as shown in Fig. 5(a). In Fig. 5(a), we set the geometric and material parameters as $d_1 = d_2 = 180$ mm, $t_1 = t_2 = 20$ mm, $a = 100$ mm, $h_1 = h_3 = 100$ mm, $h_2 = 200$ mm, $\varepsilon_1 = \varepsilon_2 = \varepsilon_3 = \varepsilon_4 = \varepsilon_5 = 8.854 \times 10^{-12}$ F/m, and $\mu_1 = \mu_2 = \mu_3 = \mu_4 = \mu_5 = 4\pi \times 10^{-7}$ H/m. Because of the symmetric distributions of electric field with respect to the u–v plane in Fig. 2, we only represented half of the resulting distribution at each frequency in Fig. 5(a). The maximum strength of the electric field at 4 GHz (approximately 18 V/m) is stronger than that at 2 GHz (approximately 14 V/m). This result implies that the installed digital modules would possibly be vulnerable to the unwanted electric-line current in the high-frequency regime. In addition, we quantitatively compared our computed results with those derived by a commercial EM simulator (COMSOL Multiphysics [15]), as shown in Fig. 5(b), in which the electric-field strength is calculated along the white dashed line ($x = -280$ mm, -300 mm $\leq z \leq 100$ mm) in Fig. 5(a), to validate our approach. In the commercial EM simulation, we modeled the closed cabinet including both digital modules using the geometrical and material parameters presented in Fig. 5, and then applied the PEC boundary to the surface of a cabinet and digital modules, as well as injected the surface current of 0.1592 ($= 1/2\pi$) A/m into a conductive cylinder with the radius of 1 mm to realize an electric-line current of 0.001 A/m². The results derived by the mode-matching analysis and a commercial simulator are similar to each other with respect to the electric-field distribution and strength. From the point of view of regulation for nuclear power plants, we can see that the electric-field strength is higher than the maximum allowable strength of the radiating electric field (10 V/m = 20 dBV/m = 140 dBμV/m) at confinable locations in Fig. 5(b), which implies that precaution against EMI should be taken [10].
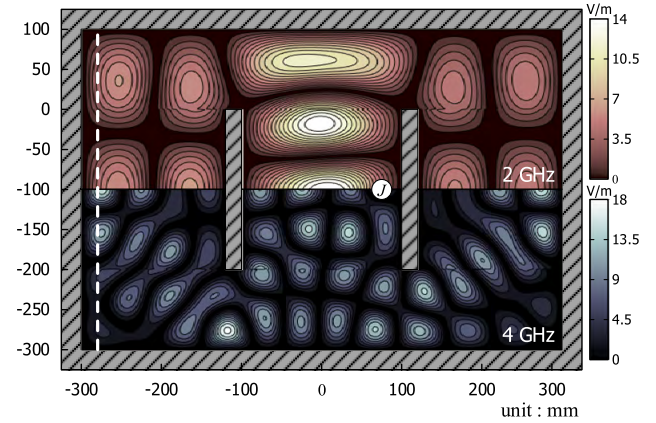
(a)
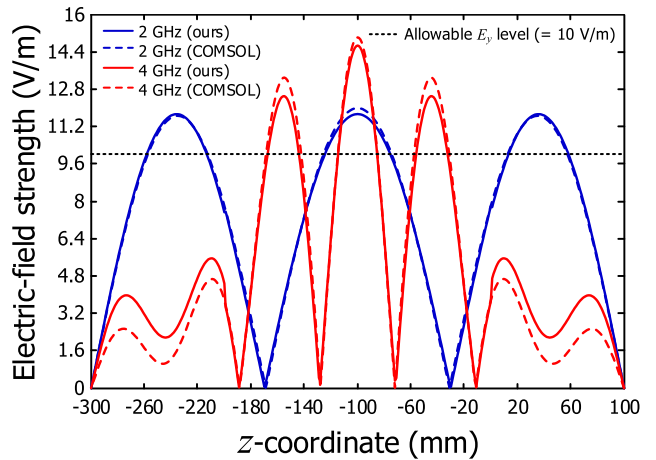
(b)

FIGURE 5. (a) Electric-field distributions and (b) electric-field strength on the white dashed line in Fig. 5(a) ($x = -280$ mm, -300 mm $\leq z \leq 100$ mm) when the electric-line current is located at ($x = x' = 70$ mm, $z = z' = -100$ m) at 2 GHz and 4 GHz ($J = 0.001$ A/m², $d_1 = d_2 = 180$ mm, $t_1 = t_2 = 20$ mm, $a = 100$ mm, $h_1 = h_3 = 100$ mm, $h_2 = 200$ mm, $\varepsilon_1 = \varepsilon_2 = \varepsilon_3 = \varepsilon_4 = \varepsilon_5 = 8.854 \times 10^{-12}$ F/m, and $\mu_1 = \mu_2 = \mu_3 = \mu_4 = \mu_5 = 4\pi \times 10^{-7}$ H/m).

Thus, we investigated the electric-field distribution in terms of the various geometric parameters such as d_1, d_2, h_1, h_2, and h_3. Noting that proper modification of the geometric parameters can effectively control the EM field generated from the undesirable current source, we focused on the interest region as the expressed scan line in Fig. 2 (depicted as a blue line) and investigated the electric-field strength of the air-filled closed cabinet along the scan line while modifying the various design parameters. To evaluate whether the electric-field strength is acceptable or not, we employed the maximum allowable strength of the radiating electric field (10 V/m) [10]. The electric-field strength on the scan line in region IV is expressed as

$$E_y^{IV}(x = x_s, z)$$

$$= i\omega \sum_{m_4=1}^{M_4} \sin \frac{\pi}{2} m_4 (A_{m_4} \sin \xi_{m_4} z + B_{m_4} \cos \xi_{m_4} z) \quad (12)$$

where $-h_2 \leq z \leq 0$, $\xi_{m_4} = \sqrt{\omega^2 \varepsilon_4 \mu_4 - (m_4\pi/d_2)^2}$.
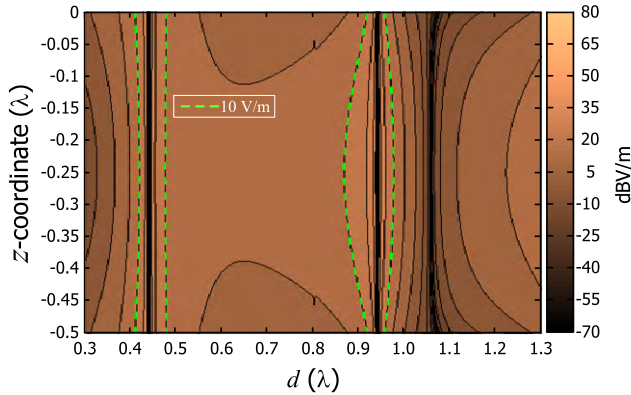
FIGURE 6. Electric-field strength on the scan line in region IV while d $(= d_1 = d_2)$ changes from 0.3 λ to 1.3 λ ($J = 0.001$ A/m^2, $h_1 = h_2 = h_3 = 0.5$ λ , $a = 0.5$ λ, $t_1 = t_2 = 0.2$ λ, and frequency = 3 GHz).

Note that the total electric-field strength in (12) is affected by the electric field of odd modes ($m_4 = 1, 3, 5, \cdots$) because of the $(\sin m_4\pi/2)$ term. For the air-filled cabinet, the propagation mode ($\xi_{m_4} \geq 0$) in region IV can be generated when d_2 is greater than 0.5 λ.

Fig. 6 shows the computed electric-field strength of the symmetrical structure with respect to the u–v and v–w planes in Fig. 2, while d ($= d_1 = d_2$) varies from 0.3 λ to 1.3 λ under the condition of $h_1 = h_2 = h_3 = 0.5$ λ, $a = 0.5$ λ, $t_1 = t_2 = 0.2$ λ, and frequency = 3 GHz. To understand why the electric field is either strong or weak in terms of d, we investigated the modal coefficients A_{m_4} and B_{m_4}, as well as the propagation constant ξ_{m_4}. We found that the electric field of the first mode ($m_4 = 1$), which depends on ($A_{m_4}\sin\xi_{m_4}z + B_{m_4}\cos\xi_{m_4}z$), dominantly influences the total electric field strength when d is greater than 0.5 λ, whereas that of the evanescent mode ($\xi_{m_4} < 0$) governs the total electric-field strength when d is smaller than 0.5 λ.

To explain Fig. 6 thoroughly, the electric-field strength increases with increasing d up to $d \approx 0.44$ λ and then decreases with opposite phase as d continues to increase over 0.44 λ. Furthermore, for the case of distance $d \approx 0.5$ λ, the total electric-field strength is mainly determined by the modal coefficient B_{m_4} of the first mode ($m_4 = 1$) because the propagation constant ξ_{m_4} of the first mode approaches zero. In the case of $d = 1.055$ λ, the total electric-field .strength is nearly zero because the electric field of the propagation mode ($m_4 = 1$) and the electric field of the evanescent mode ($m_4 = 3$) cancel out each other.

We derived the electric-field strength of the asymmetric structure by changing either the ratio d_1 / d_2 or the ratio h_3 / h_1. Fig. 7 shows the electric-field strength on the scan line when the ratio d_1 / d_2 ($d_1 = 0.9$ λ) increases from 0.3 to 2.3. Fig. 7 shows that the electric-field strength repeatedly changes with a period P of 0.587, increasing with a phase of 90° and decreasing with a phase of −90° . Similarly, after checking the results for other cases with a different distance d_1, we confirmed that the period P is inversely proportional to d_1 in region II. This result indicates that the adjustment of d_1 in the region II can be a possible way
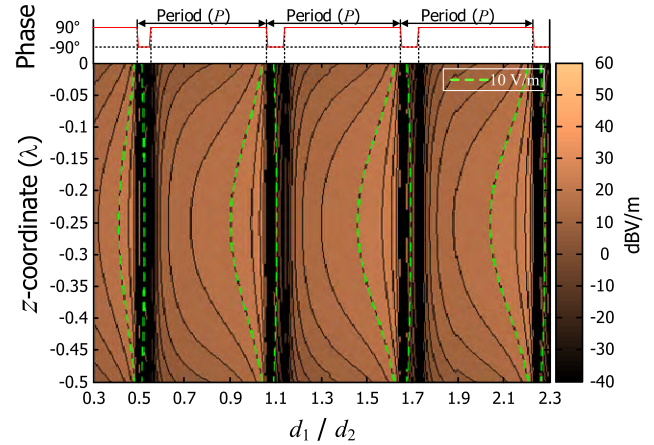

FIGURE 7. Electric-field strength on the scan line while the ratio d_1 / d_2 changes from 0.3 to 2.3 ($J = 0.001$ A/m^2, $d_2 = 0.9$ λ, $h_1 = h_2 = h_3 = 0.5$ λ, $a = 0.5$ λ, $t_1 = t_2 = 0.2$ λ, and frequency = 3 GHz).
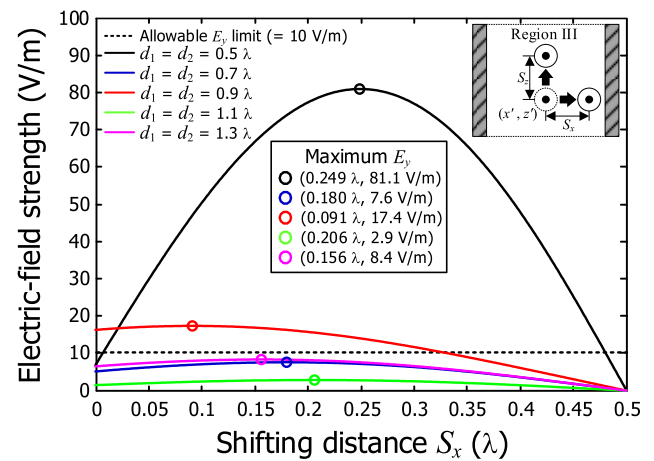

FIGURE 8. Electric-field strength at the observation point $P_o(x_o = x_s,$ $z_o = -h_2 / 2)$ while the current source shifts along the x-direction ($J = 0.001$ A/m^2, $h_1 = h_2 = h_3 = 0.5$ λ, $a = 0.5$ λ, $t_1 = t_2 = 0.2$ λ, and frequency = 3 GHz).

to control the EMI from the unwanted electric-line current. Additionally, we investigated the variation in electric-field strength on the scan line as the ratio h_3 / h_1 varies for the same structure in Fig. 7. The resulting electric-field strength drastically changes depending on the z-coordinate on the scan line and the ratio h_3 / h_1. We think that is because the electric fields generated in regions I and V considerably influence the electric-field distribution in region IV.

Next, we investigated the variation in the electric-field strength at observation point P_o in Fig. 2 (depicted as a red point), corresponding to the change in the current source position ($x = x'$, $z = z'$) with respect to the cabinet, symmetrical to the u–v and v–w planes, as shown in Fig. 2 (illustrated in the inset of Fig. 8). Fig. 8 shows the calculated electric-field strength at observation point P_o for the cases with different distances d_1 ($= d_2$) as the shifting distance S_x, shown in the inset in Fig. 8, increases to 0.5 λ. Note that the strongest electric field is generated at observation point P_o owing to its symmetry in the case that the current
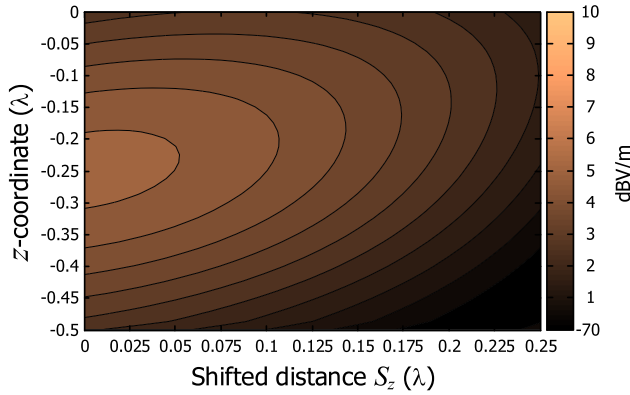
FIGURE 9. Electric-field strength on the scan line as the current source shifts along the z-direction ($J = 0.001$ A/m^2, $h_1 = h_2 = h_3 = 0.5$ λ, $a = 0.5$ λ, $t_1 = t_2 = 0.2$ λ, frequency = 3 GHz).

source shifts along the *x*-direction. The resulting electric-field strength for each case increases and then decreases after reaching the maximum electric-field strength, as depicted by the circular markers in Fig. 8. We think that is because the adjustment of the current source position modifies the electric field penetrating into region IV from region III. Considering the allowable electric-field strength of 10 V/m, Fig. 8 shows that the both cases with $d_1 = d_2 = 0.5$ λ and $d_1 = d_2 = 0.9$ λ are not recommended in the design of the closed cabinet because the electric-field strength exceeds 10 V/m.

As shown in Fig. 9, we finally investigated the electric-field strength on the scan line as function of shifting distance S_z (as depicted in the inset of Fig. 8) for the case with $d_1 = d_2 = 0.7$ λ in Fig. 8. As the shifting distance S_z increases, the electric-field strength slowly decreases in Fig. 9. This implies that the influence of the electric field penetrating into region IV is reduced as the current source approaches region I. Furthermore, the contours of the electric-field strength in Fig. 9 tilt toward the *z*-direction, which is caused by the shift in the current source *z*-direction.

IV. CONCLUSION

We applied the mode-matching method to the electromagnetic analysis of a closed cabinet to prevent the EMI problems caused by an internal parasitic current source. In the mode-matching method, we utilized both the superposition principle and Helmholtz equation in conjunction with the separation of variables to express the electromagnetic field. The boundary conditions for the tangential electric- and magnetic-field continuities between the separated regions were enforced to obtain the modal coefficient in each region. The modal coefficients derived from a set of simultaneous equations were employed to predict how much the electric and magnetic fields generated by the electric-line current interfere with nearby regions as a function of geometric parameters. The investigated electric-field distributions provide us with useful information to mitigate the EMI geometrically from the electric-line current source. Furthermore, the presented results can offer practical guidance regarding

chassis design for the installation of digital modules with immunity to EMI.

APPENDIX

Here, we specifically describe the continuity conditions of the tangential E_y and H_x at $z = 0$ to derive the simultaneous equations. First, the tangential E_y continuity at $z = 0$ is expressed as (7). By multiplying (7) by $\sin \gamma_{p_1}(x - x_9)$ and then integrating the result with respect to *x* from x_9 to x_{10}, we obtain

$$
i\omega \sum_{m_1=1}^{M_1} A_{m_1} \sin \xi_{m_1}(-z_9)
$$
$$
\times \left(\int_{x_9}^{x_{10}} \sin \gamma_{m_1}(x - x_9) \sin \gamma_{p_1}(x - x_9) dx \right)
$$
$$
= i\omega \sum_{m_2=1}^{M_2} B_{m_2} \left(\int_{x_9}^{x_1} \sin \gamma_{m_2}(x - x_9) \sin \gamma_{p_1}(x - x_9) dx \right)
$$
$$
+ i\omega \sum_{m_3=1}^{M_3} B_{m_3} \left(\int_{x_2}^{x_3} \sin \gamma_{m_3}(x - x_2) \sin \gamma_{p_1}(x - x_9) dx \right)
$$
$$
+ i\omega \sum_{m_4=1}^{M_4} B_{m_4} \left(\int_{x_4}^{x_{10}} \sin \gamma_{m_4}(x - x_4) \sin \gamma_{p_1}(x - x_9) dx \right)
$$
(A1)

where $p_1 = \gamma_{p_1} = p_1\pi/(x_{10} - x_9) = p_1\pi / (2a + t_1 + t_2 + d_1 + d_2)$.

(A1) is simply represented as

$$
\sum_{m_1=1}^{M_1} \frac{A_{m_1}(x_9 - x_{10}) \sin \xi_{m_1} z_9}{2} \delta_{m_1 p_1}
$$
$$
= \sum_{m_2=1}^{M_2} B_{m_2} F(x_9, x_1, x_9, \gamma_{m_2}, \gamma_{p_1})
$$
$$
+ \sum_{m_3=1}^{M_3} B_{m_3} F(x_2, x_3, x_9, \gamma_{m_3}, \gamma_{p_1})
$$
$$
+ \sum_{m_4=1}^{M_4} B_{m_4} F(x_4, x_{10}, x_9, \gamma_{m_4}, \gamma_{p_1})
$$
(A2)

where $F(a, b, c, m_\alpha, p_\beta) = \int_a^b \sin m_\alpha(x - a) \sin p_\beta(x - c)dx$.

Second, the continuities of the tangential H_x at $z = 0$ are expressed as (8)–(10). We express only (8) for the boundary between regions I and II because the description for both (9) and (10) is analogous to that for (8). Multiplying (8), which is the continuity of the tangential H_x at $z = 0$ in the range from x_9 to x_1, by $\sin \gamma_{p_2}(x - x_9)$ and then integrating the result with respect to *x* from x_9 to x_1 yields

$$
\frac{1}{\mu_1} \sum_{m_1=1}^{M_1} A_{m_1} \xi_{m_1} \cos \xi_{m_1} z_9
$$
$$
\times \left(\int_{x_9}^{x_1} \sin \gamma_{m_1}(x - x_9) \sin \gamma_{p_2}(x - x_9) dx \right)
$$

$$= \frac{1}{\mu_2} \sum_{m_2=1}^{M_2} A_{m_2} \xi_{m_2}$$

$$\times \left(\int_{x_9}^{x_1} \sin \gamma_{m_2}(x-x_9) \sin \gamma_{p_2}(x-x_9) dx \right) \tag{A3}$$

where $\gamma_{p_2} = p_2 \pi / (x_1 - x_9) = p_2 \pi / d_1$.

(A3) is simply expressed as

$$\sum_{m_1=1}^{M_1} 2A_{m_1} \mu_2 \xi_{m_1} F(x_9, x_1, x_9, \gamma_{p_2}, \gamma_{m_1}) \cos \xi_{m_1} z_9$$

$$= \sum_{m_2=1}^{M_2} A_{m_2} \mu_1 \xi_{m_2}(x_1 - x_9)\delta_{m_2 p_2}. \tag{A4}$$

According to (9), (10) and the conditions of the tangential E_y and H_x at $z = -h_2$, the specific derivations are analogous to the aforementioned explanation.

REFERENCES

[1] M.-G. Min, J.-K. Lee, Y.-H. Ji, S.-H. Jo, and H.-J. Kim, "Evaluation of electromagnetic interference environment of the instrumentation and control systems in nuclear power units," *Nucl. Eng. Design*, vol. 285, pp. 15–22, Apr. 2015.

[2] T.-P. Wang and Z.-W. Li, "Significant reduction of electromagnetic interference for fine-motion control rod drive in a nuclear reactor," *IEEE Trans. Ind. Electron.*, vol. 61, no. 10, pp. 5582–5589, Oct. 2014.

[3] P. F. Keebler and S. Berger, "Going from analog to digital—Radiated emissions performance of a nuclear plant control system from 10 kHz to 6 GHz," in *Proc. 10th Int. Symp. EMC*, York, U.K., 2011, pp. 373–379.

[4] J. Choo, C. Jeong, and J. Choo, "Transverse electric scattering of open cabinet in nuclear power plants," *IEEE Antennas Wireless Propag. Lett.*, vol. 15, pp. 1204–1207, Apr. 2016.

[5] J. Choo, J. Choo, and Y.-H. Kim, "Shielding effectiveness of open cabinet containing digital modules using ferrite sheet," *IEEE Trans. Magn.*, vol. 53, no. 12, Dec. 2017, Art. no. 2900609.

[6] F. Nekoogar and F. Dowla, "Design considerations for secure wireless sensor communication systems in harsh electromagnetic environments of nuclear reactor facilities," *Nucl. Technol.*, vol. 202, pp. 191–200, Apr. 2018.

[7] J.-E. Park, J. Choo, and H. Choo, "Electromagnetic scattering of periodic cabinets in nuclear power plants: Parallel polarization," *IEEE Access*, vol. 7, pp. 16487–16493, Jan. 2019.

[8] M.-G. Min, J.-K. Lee, K.-H. Lee, and D. Lee, "Proposing a low-frequency radiated magnetic field susceptibility (RS101) test exemption criterion for NPPs," *Nucl. Eng. Technol.*, to be published.

[9] *Guidelines for Electromagnetic Interference Testing of Power Plant Equipment: Revision 3*, document TR-102323, EPRI, Palo Alto, CA, USA, Nov. 2004.

[10] *Guidelines for Evaluating Electromagnetic and Radio-Frequency Interference in Safety-Related Instrumentation and Control Systems, Revision 1*, U.S. NRC, Rockville, MD, USA, Oct. 2003.

[11] *Requirements for the Control of Electromagnetic Interference Characteristics of Subsystems and Equipment*, Standard MIL-461E, Department of Defense Interface Standard, USA, Aug. 1990.

[12] D. I. Yang, H. J. Eom, and J. W. Ra, "Radiation from groove-backed antennas with a gap," *IEEE Antennas Wireless Propag. Lett.*, vol. 3, no. 1, pp. 208–210, Dec. 2004.

[13] H. J. Eom, *Wave Scattering Theory*. Berlin, Germany: Springer Verlag, 2001, ch. 8–9, pp. 181–233.

[14] J. Choo, J. Choo, and Y. H. Kim, "Evaluation of electromagnetic interference from axially ruptured coaxial cable with multiple dielectrics used in nuclear power plants," *IEEE Trans. Electromagn. Compat.*, to be published.

[15] *COMSOL Multiphysics 5.4*. Accessed: May 8, 2019. [Online]. Available: https://www.comso

JAEYUL CHOO received the B.S. and M.S. degrees in electronic and electrical engineering from Hongik University, Seoul, South Korea, in 2004 and 2006, respectively, and the Ph.D. degree in electrical engineering from the Korea Advanced Institute of Science and Technology (KAIST), Daejeon, South Korea, in 2014. He was an Associate Research Engineer with the Central Research and Development Center, LS Industrial Systems Company, Ltd., Anyang, South Korea, from 2006 to 2010. In 2014, he joined the Korea Institute of Nuclear Safety, Daejeon. His current research interests include the design of tag and reader antennas for RFID, the electrical analysis for flip-chip bonding package, and the electromagnetic field analyses of vias, transmission lines, and scattering structure for dealing with electromagnetic interference problems.

JONG-EON PARK received the B.S., M.S., and Ph.D. degrees from the School of Electrical Engineering and Computer Science from Kyungpook National University, Daegu, South Korea, in 2006, 2009, and 2013, respectively. From 2013 to 2015, he was a Postdoctoral Researcher with The Ohio State University. Since 2016, he has been with Hongik University, where he is currently a Research Professor with the Metamaterial Electronic Device Research Center. His research interests include scattering phenomena through aperture, antenna design, and computational electromagnetics.

HOSUNG CHOO received the B.S. degree in radio science and engineering from Hanyang University, Seoul, South Korea, in 1998, and the M.S. and Ph.D. degrees in electrical and computer engineering from the University of Texas at Austin, in 2000 and 2003, respectively. In 2003, he joined the School of Electronic and Electrical Engineering, Hongik University, Seoul, where he is currently a Professor. His research interests include electrically small antennas for wireless communications, reader and tag antennas for RFID, on-glass and conformal antennas for vehicles and aircraft, and array antennas for GPS applications.

YONG-HWA KIM received the B.S. degree in electrical engineering and the Ph.D. degree in electrical and computer engineering from Seoul National University, Seoul, South Korea, in 2001 and 2007, respectively. From 2007 to 2011, he was a Senior Researcher with the Korea Electrotechnology Research Institute (KERI), Geonggi-do, South Korea. From 2011 to 2013, he was an Assistant Professor with the Division of Maritime Electronic and Communication Engineering, Mokpo National Maritime University, South Korea. Since 2013, he has been a Faculty with the Department of Electronic Engineering, Myongji University, South Korea. His general research interests include communication systems, fault diagnosis, and digital signal processing. He is particularly interested in communications and artificial intelligence for smart grid.

● ● ●